(Preprint) AAS 24-123

PRESCRIBED MOTION DYNAMICS FOR SPACECRAFT SOLAR ARRAY DEPLOYMENT

Leah Kiner[*], Cody Allard[†] and Hanspeter Schaub[‡]

In the early stages of any spacecraft mission, the importance of verifying mission requirements through extensive simulation and subsequent analysis cannot be understated. As concepts for space vehicles and their attached appendages continue to grow in complexity, the ability to rapidly model these spacecraft designs and simulate the dynamical impacts between components becomes critical for mission success and reliability of the selected spacecraft design. Previous work developed a prescribed motion dynamics module in the Basilisk astrodynamics simulation framework that enabled simulation of the dynamics between a *single* rigid body connected to a rigid spacecraft hub. The connected rigid body's full kinematic motion was prescribed using additional translational and rotational profiler modules. This work expands the capability of these software tools to simulate spacecraft components with *multiple* connected rigid elements. The advancement of spacecraft solar array designs from small-scale single-hinged rigid panels to immense, precisely articulable flexible-substrate arrays is the focus of this work. By considering each solar array as a collection of N connected rigid elements, the previously developed prescribed motion dynamics module is used to simulate the dynamics of each element acting on the spacecraft hub. N instances of both the translational and rotational kinematic profiler modules are used to profile the kinematic states of each array element relative to the spacecraft hub. The dynamical impact of several array deployment configurations on the spacecraft hub is shown and compared for each deployment scenario. The deployment modeling methodology presented in this work provides general reconfiguration solutions that are not specific to a single design, but rather can model a family of deployable subcomponents.

INTRODUCTION

Effective modeling and simulation of complex spacecraft concepts is crucial for the success of any space mission. Particularly in the early phases of spacecraft mission design, the ability to rapidly model a wide range of complex spacecraft configurations in a generalized way is paramount to analyze and verify mission requirements. Further, as mission concepts continue to evolve and become more ambitious, the spacecraft designs required to fulfill the goals of such missions also grow with increasing complexity. For example, to meet the needs of deep-space missions such as

[*]Graduate Research Assistant, Ann and H.J. Smead Department of Aerospace Engineering Sciences, University of Colorado Boulder, Colorado Center For Astrodynamics Research, Boulder, CO, 80303 USA. leah.kiner@colorado.edu

[†]Guidance, Navigation and Control Engineer, Laboratory for Atmospheric and Space Physics, University of Colorado Boulder, Boulder, CO, 80303 USA

[‡]Professor and Department Chair, Schaden Leadership Chair, Ann and H.J. Smead Department of Aerospace Engineering Sciences, University of Colorado, Boulder, 431 UCB, Colorado Center for Astrodynamics Research, Boulder, CO, 80309. AAS Fellow, AIAA Fellow.

Deep Space 1[1] , Dawn,[2] and Psyche,[3] spacecraft ionic thruster designs have advanced from hub-fixed configurations to being mounted on gimbaled platforms[4,5] to account for offsets between the spacecraft center of mass and the thrust vector.[5,6] Advancements in orbital servicing and docking operations have driven the development of multi-link robotic arms such as the Canadarm[7–9] that was used on the Space Shuttle and the ISS. Similar advancements in complexity have been seen for spacecraft solar power systems, which is central to the motivation of this work.

Spacecraft solar power systems[10] have seen a drastic evolution since the launch of the first solar powered Vanguard 1 spacecraft in 1958. Launched with just six body-mounted solar cells producing only a single watt of power, Vanguard 1 marked the beginning of solar-powered spacecraft development. Within the next year, solar powered designs advanced to strut-mounted solar "paddles" seen first on Pioneer 5 which later advanced to deployable fixed-orientation solar panels beginning in 1961 with the Ranger series and the Lunar Orbiter 1 in 1966. By 1973, the US launched Mariner 10, the first two-wing gimbaled solar array design that enabled tracking of the Sun. This concept, together with the cheaper hub-fixed panel design, remain in primary use today. The latest missions to the farthest edges of our solar system such as the Lucy mission to the Trojan asteroids and the DART binary asteroid impact mission have required extensive solar powered advancements to meet higher power needs. The Lucy mission uses two large circular flexible-substrate solar arrays which deploy using a rotational motor-driven lanyard[11,12] and articulate to track the Sun. The DART spacecraft also uses flexible-substrate solar arrays, however the two rectangular arrays deploy using a roll-out method.

Inspired by the deployment mechanisms seen in the Lucy and DART missions, this work focuses on modeling similar solar array deployment mechanisms in the Basilisk* astrodynamics simulation software architecture. The spacecraft-centric, modular implementation of the spacecraft dynamics and flight software modules enables rapid simulation of a wide variety of spacecraft configurations that can be integrated easily with reaction wheels, thrusters, or fuel tank sloshing. Exploiting the modularity of Basilisk, the existing capability to simulate a rigid body following prescribed motion[13,14] relative to a central spacecraft hub is expanded to simulate the solar array deployment scenarios. To demonstrate the applicability and versatility of the developed simulation software tools, this paper considers four distinct solar array deployment scenarios. The space vehicle in all scenarios consists of a central rigid hub with two symmetrically attached solar arrays. Each solar array is modeled as a collection of N rigid elements. All four scenarios deploy the arrays individually rather than simultaneously to reflect a single mission design choice. Two scenarios illustrate the circular rotational array deployment seen in Fig. (1). The second two scenarios illustrate the telescoping solar panel deployment seen in Fig. (2).

For all deployment scenarios, the array elements are initially oriented in a stowed configuration where they are stacked together into a wedge-like shape. The stowed configuration for both rotational deployment scenarios are identical and shown in Fig. 1(a). The stowed configurations for the telescoping scenarios are also identical and are shown in Fig. 2(a). Further, each array deploys in two stages. The first stage is the *initial deployment phase* where the stacked elements rotate together from the stowed configuration away from the spacecraft hub into the initial deployment configuration. The initial array 1 deployment configurations for each scenario are illustrated in Figs. 1(b) and 2(b). The initial deployment configurations for array 2 are shown in Figs. 1(d) and 2(d). The second stage is the *main deployment stage* where the elements begin to unfurl to their deployed locations. The configurations with both arrays fully deployed are illustrated in Figs. 1(e) and 2(e),

*`https://hanspeterschaub.info/basilisk`

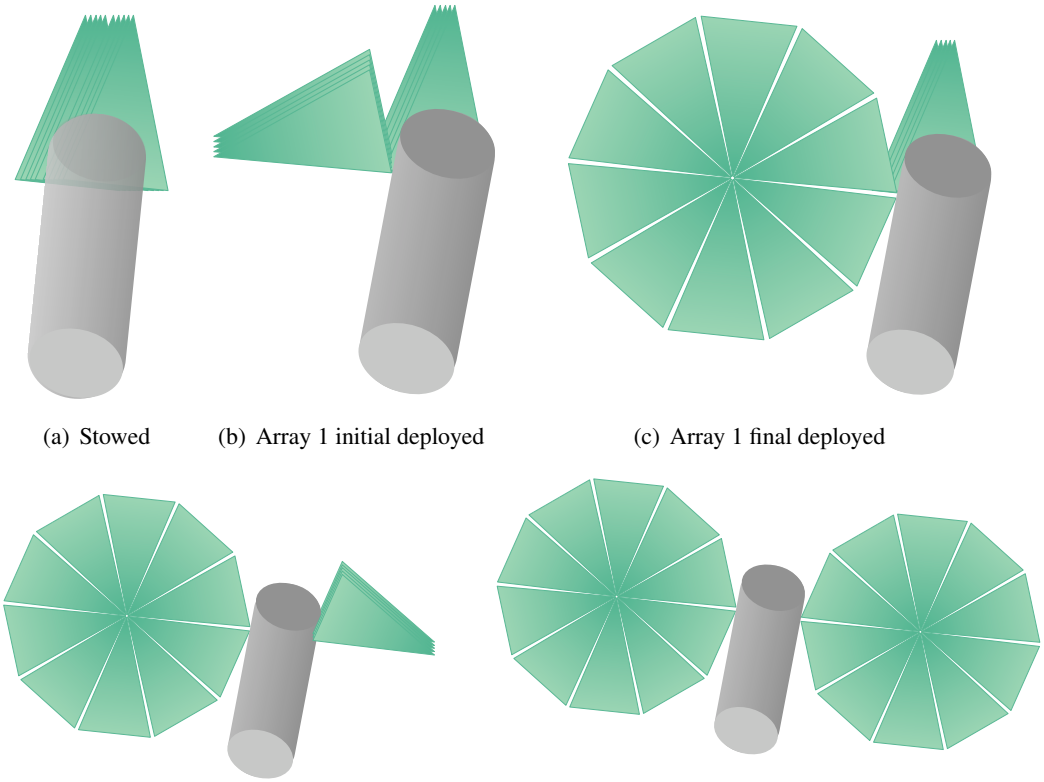

(a) Stowed (b) Array 1 initial deployed (c) Array 1 final deployed

(d) Array 2 initial deployed (e) Array 2 final deployed

Figure 1. Solar array configurations for the rotational deployment scenarios.

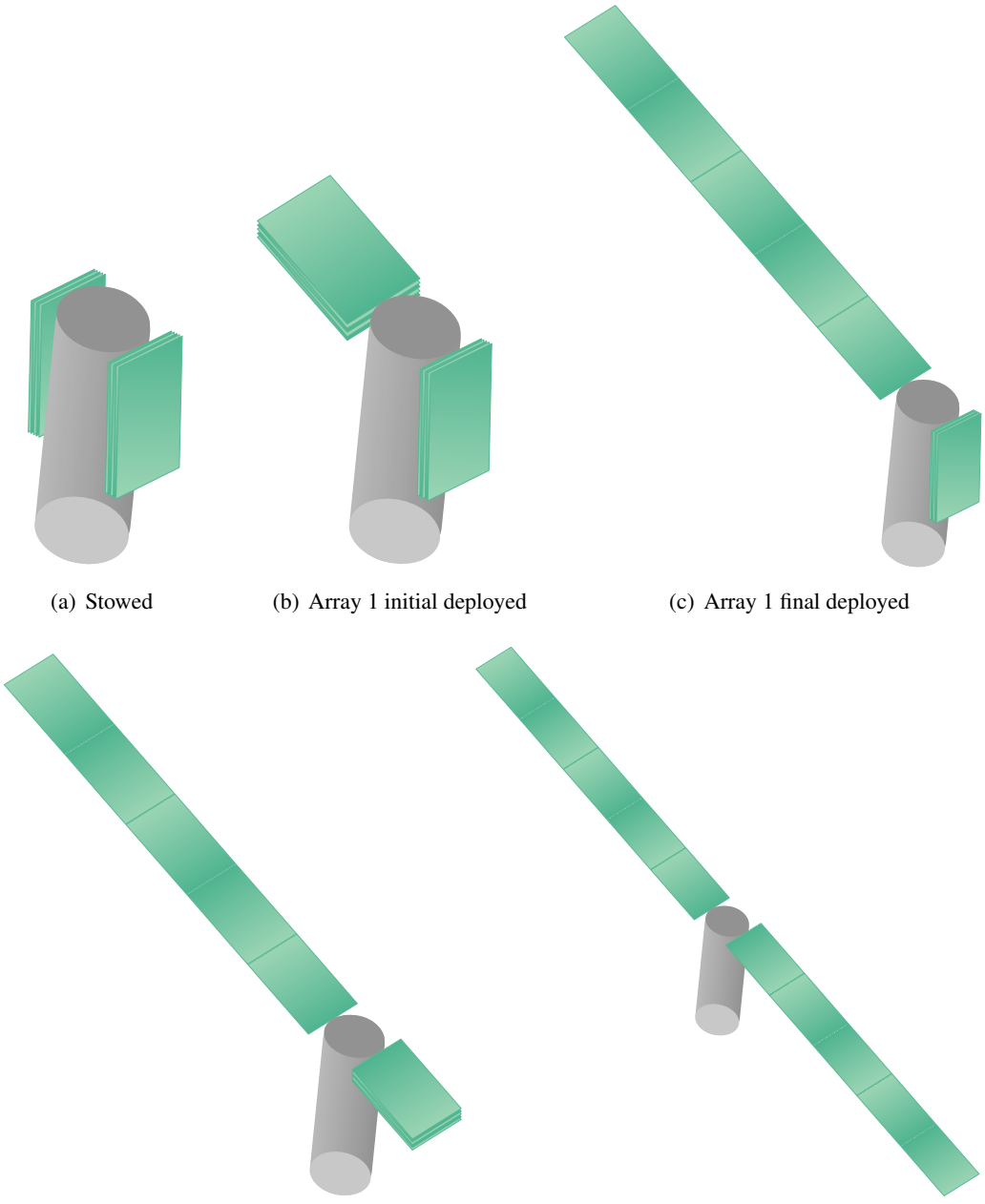

(a) Stowed (b) Array 1 initial deployed (c) Array 1 final deployed

(d) Array 2 initial deployed (e) Array 2 final deployed

Figure 2. Solar array configurations for the telescoping deployment scenarios.

respectively.

The first rotational scenario demonstrates a purely rigid deployment and the other imitates the time-varying lanyard deployment used in the Lucy mission. Similarly, the telescoping deployment scenarios demonstrate both a rigid deployment and a time-varying lanyard deployment. The lanyard deployment scenarios are a best attempt to imitate the time-varying nature of solar arrays deployed using a motor-driven lanyard. To mimic this type of deployment, all array elements begin to move at the start of the main deployment phase. The elements synchronously lock into their final positions at the end of the main deployment phase. This method of deployment contrasts with the rigid deployments, where the stacked elements lock into place at different intervals throughout the deployment. The elements in the rigid rotational deployment scenario rotate together throughout the deployment and individually lock into place at regular intervals until the array is fully deployed. The elements in the rigid telescoping deployment scenario instead remain stacked in the initial deployment configuration while each element is individually pushed away from the hub at regular intervals until the panel is fully deployed.

The structure of this paper is as follows. First, an overview of each deployment scenario is given with the required frame definitions and parameters for the spacecraft and solar array models. Second, the previously derived prescribed motion dynamics required to simulate the deployment scenarios are presented. Next, the software implementation of the spacecraft dynamics using the Basilisk astrodynamics simulation framework is discussed and an overview of the kinematic translational and rotational modules used to profile the motion of each individual array element is given. Finally, the simulation setup for each deployment scenario is presented in the results section along with the simulation results for each of the four scenarios. The profiled array element states are shown and the effect of the deployment on the hub rotational motion is presented and compared for each deployment scenario.

PROBLEM STATEMENT

The array deployment scenarios in this work consider a space vehicle consisting of a rigid hub and two identical solar arrays that are each modeled as a collection of N rigid elements. The spacecraft geometry and required frame definitions for the rotational deployment scenarios are illustrated in Fig (3). The frame information for the telescoping deployment scenarios is illustrated in Fig (4). Figure 3(a) illustrates the stowed frame orientations for the rotational deployment scenarios and 3(b) presents both array initial deployment configurations for clarity. Both arrays are included in the latter figure for the purpose of compactness. Similarly, Fig. 4(a) illustrates the stowed frame orientations for the telescoping deployment scenarios. Figure 4(b) presents two deployed array 2 elements where $N = 2$ to clarify the frame orientations for the main telescoping deployment phase. Array 1 is not presented for both compactness and simplicity in this scenario geometry.

For all scenarios, the rigid hub body frame is denoted $\mathcal{B} : \{B, \hat{\boldsymbol{b}}_1, \hat{\boldsymbol{b}}_2, \hat{\boldsymbol{b}}_3\}$ and is located at the hub center of mass point B_c. The solar arrays are symmetrically mounted to the hub at the hub-fixed points M_1 and M_2. Solar array 1 is designated as the array mounted along the positive $\hat{\boldsymbol{b}}_1$ axis. Each individual array element's kinematic motion is profiled relative to a hub-fixed mount frame denoted as $\mathcal{M}_i : \{M_i, \hat{\boldsymbol{m}}_{i_1}, \hat{\boldsymbol{m}}_{i_2}, \hat{\boldsymbol{m}}_{i_3}\}$ where $i = 1, 2$. The mount frames in all deployment scenarios have the same orientation as the spacecraft body frame, as seen in Figs. (3) and (4). Therefore, the angular velocity of each mount frame with respect to the hub frame $\boldsymbol{\omega}_{\mathcal{M}_i/\mathcal{B}}$ is fixed at zero for all deployment scenarios.

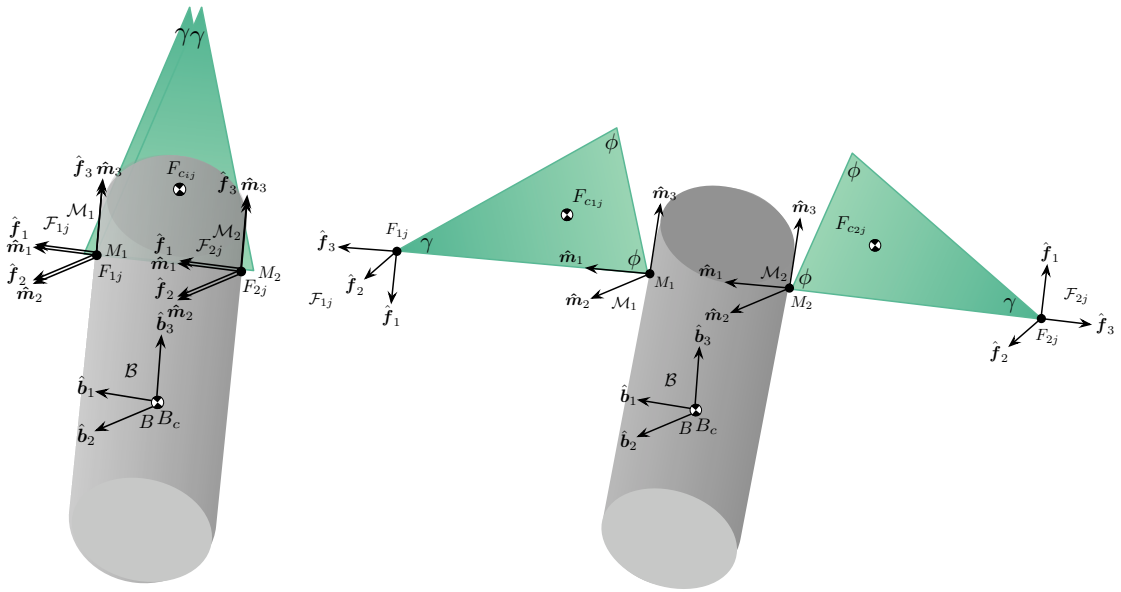

(a) Stowed configuration

(b) Initial deployed configuration

Figure 3. Rotational deployment scenario frame definitions.

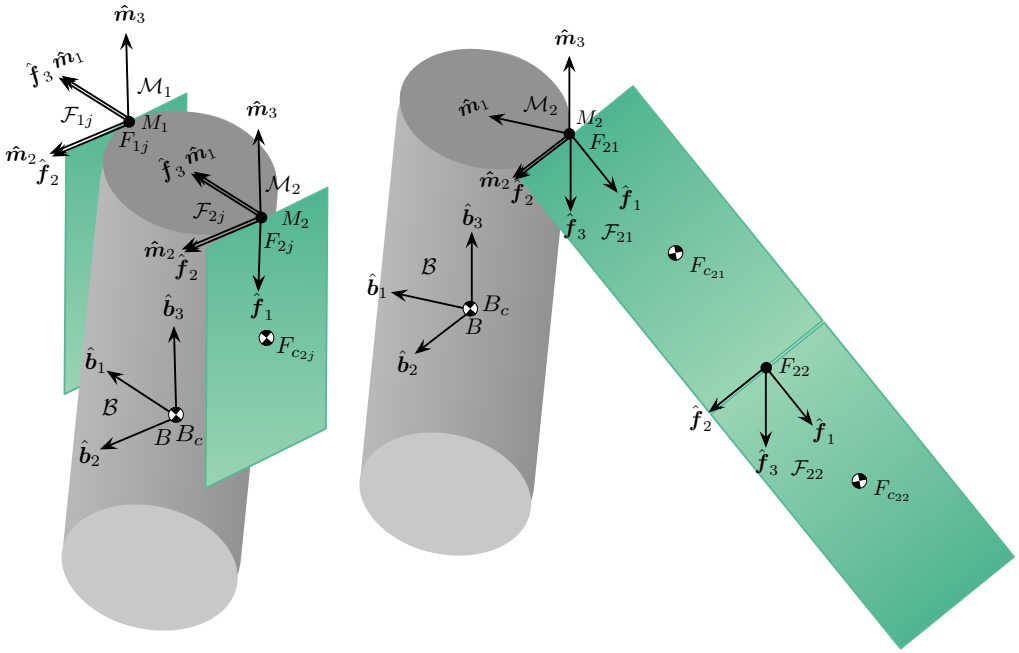

(a) Stowed configuration

(b) Array 2 deployed configuration for $N = 2$

Figure 4. Telescoping deployment scenario frame definitions.

The body frame of each rigid element is denoted $\mathcal{F}_{ij} : \{F_{ij}, \hat{\boldsymbol{f}}_{ij_1}, \hat{\boldsymbol{f}}_{ij_2}, \hat{\boldsymbol{f}}_{ij_3}\}$ where $j = 1 \cdots N$ denotes the jth array element and $i = 1, 2$ for each solar array. Accordingly, the translational and rotational motion of each array element is profiled using the array element body frames $\mathcal{F}_{ij}$ relative to their respective mount frame $\mathcal{M}_i$. The rotation axis for each array in all scenarios is identical and is denoted ${}^{\mathcal{M}_i}\hat{\boldsymbol{s}}$. The axis of translation for the translational scenarios is denoted ${}^{\mathcal{M}_i}\hat{\boldsymbol{t}}$ for each array. The following sections describe each individual deployment scenario in further detail.

Rotational Deployment Scenarios

This section discusses the relationship between the defined frames for the rotational deployment scenarios in greater detail. Knowledge of initial frame orientations, point locations, and the required array element positions and attitudes relative to the spacecraft hub during deployment is necessary for implementing these scenarios in the Basilisk software. Recall the spacecraft geometry and frame definitions seen in Fig. (3) for the rotational deployment scenarios.

It is important to note that for these scenarios to be configured using the existing Basilisk profiler modules, the array element frames must either purely translate or purely rotate with respect to their respective mount frames. By re-configuring the element frames after the initial deployment phase to be located at the centroid of each deployed array as seen in Fig. 3(b), the array element states can be profiled using a purely 1 DOF rotational motion profiler. This frame re-configuration ensures that the element translational states remain constant relative to their respective mount frames throughout all deployment phases.

Stowed Configuration

In the stowed configuration seen in Fig. 3(a), first the center of mass location of each array element must be defined in element frame components as the centroid of the triangular wedge as:

$$ {}^{\mathcal{F}_{ij}}\boldsymbol{r}_{F_{ij_c}/F_{ij},\text{stowed}} = \begin{bmatrix}(-1)^i R\cos(\phi), & 0.0, & \frac{R}{3}\sin(\phi)\end{bmatrix}^T \tag{1}$$

where R is the radius of each solar array, $j = 1 \cdots N$ denotes the jth array element, and $i = 1, 2$ for each solar array. The interior array angles seen in Fig. (3) are:

$$\phi = 90^\circ - \frac{\gamma}{2} \tag{2}$$

$$\gamma = \frac{360^\circ}{N} \tag{3}$$

The initial array element positions relative to the hub are defined as:

$$ {}^{\mathcal{M}_i}\boldsymbol{r}_{F_{ij}/M_i,\text{stowed}} = \begin{bmatrix}0.0, & 0.0, & 0.0\end{bmatrix}^T \tag{4}$$

Next, the initial orientation of each array element must be defined relative to their respective array mount frame. Because all array elements are initially stacked together in the stowed configuration, only a single attitude needs to be determined to describe all element orientations. Viewing Fig. 3(a), it is clear that all element frames for both solar arrays are initially aligned with their respective mount frames. Therefore, the attitude of each element frame can be described using the following Principal Rotation Vector (PRV):[15]

$$ {}^{\mathcal{M}_i}\boldsymbol{\gamma}_{\mathcal{F}_{ij}/\mathcal{M}_i,\text{stowed}} = \theta_{ij,\text{stowed}}\, {}^{\mathcal{M}_i}\hat{\boldsymbol{s}} = \theta_{ij,\text{stowed}}\, {}^{\mathcal{M}_i}\begin{bmatrix}0\\1\\0\end{bmatrix} \tag{5}$$

where

$$\theta_{ij,\text{stowed}} = 0^\circ \tag{6}$$

Initial Deployment Phase

During the initial deployment phase for array 1, the array elements rotate together from the stowed configuration seen in Fig. 1(a) to the initial deployed configuration seen in Fig. 1(b). Similarly, array 2 rotates from its stowed configuration seen in Fig 1(c) to its initial deployed configuration seen in Fig. 1(d). During their respective initial deployment phases, the array 1 elements rotate together by +90 degrees about the array 1 $\hat{\boldsymbol{m}}_2$ axis and the array 2 elements rotate together by -90 degrees about the array 2 $\hat{\boldsymbol{m}}_2$. Therefore, the attitude of each element frame at the completion of the initial deployment phase can be described for each array using the PRV:

$${}^{\mathcal{M}_i}\boldsymbol{\gamma}_{\mathcal{F}_{ij}/\mathcal{M}_i,\text{init deploy}} = \theta_{ij,\text{init deploy}}{}^{\mathcal{M}_i}\hat{\boldsymbol{s}} = \theta_{ij,\text{init deploy}}{}^{\mathcal{M}_i}\begin{bmatrix}0\\1\\0\end{bmatrix} \tag{7}$$

where

$$\theta_{ij,\text{init deploy}} = (-1)^{i+1}90^\circ \tag{8}$$

Note that because the array elements purely rotate during the initial deployment phase, their translational positions remain fixed to the vectors expressed in Eq. (4).

Main Deployment Phase

At the start of the main deployment phase for each array, the array element frames are re-configured and placed at the centroid location of each deployed solar array. This frame shift is shown in Fig. 3(b) for both arrays Therefore, the center of mass location of each array element must be updated to reflect this frame change:

$${}^{\mathcal{F}_{ij}}\boldsymbol{r}_{F_{ij_c}/F_{ij},\text{deploy}} = \left[\tfrac{2R}{3}(-1)^i\cos(\phi)\sin\left(\tfrac{\gamma}{2}\right),\quad 0.0,\quad \tfrac{2R}{3}(-1)^i\cos(\phi)\cos\left(\tfrac{\gamma}{2}\right)\right]^T \tag{9}$$

Further, because the element frame origins are now fixed at the centroid of each array relative to the hub, the element frame locations relative to the hub must also be updated:

$${}^{\mathcal{M}_i}\boldsymbol{r}_{F_{ij}/M_i} = \left[(-1)^{i+1}R,\quad 0.0,\quad 0.0\right]^T \tag{10}$$

Once deployment is complete, the attitude of each array element relative to their respective array mount frame are described by the PRVs:

$${}^{\mathcal{M}_i}\boldsymbol{\gamma}_{\mathcal{F}_{ij}/\mathcal{M}_i,\text{deploy}} = \theta_{ij,\text{deploy}}\hat{\boldsymbol{m}}_2 = \theta_{ij,\text{deploy}}{}^{\mathcal{M}_i}\begin{bmatrix}0\\1\\0\end{bmatrix} \tag{11}$$

where

$$\theta_{ij,\text{deploy}} = (-1)^{i+1}\left(90^\circ + (j-1)\gamma\right) \tag{12}$$

Telescoping Deployment Scenarios

Next, recall the spacecraft geometry and frame definitions seen in Fig. (4) for the telescoping deployment scenarios. Because each array element is rigid, the center of mass location of each array element is simply defined as the centroid of the rectangular panel along the $\boldsymbol{f}_1$ body axis:

$$^{\mathcal{F}_{ij}}\boldsymbol{r}_{F_{ij_c}/F_{ij}} = \begin{bmatrix}\frac{L}{2}, & 0.0, & 0.0\end{bmatrix}^T \tag{13}$$

where L is the fixed length of all array elements. Note that because no frame re-configuration is needed for the telescoping scenarios, this vector is constant throughout all deployment phases.

Stowed Configuration

In the stowed configuration seen in Fig. 4(a), the array element frames are coincident with the array mount frames. Therefore, the initial position of each array element is zero as in Eq. (4). The orientation of all array element frames is +90 degrees relative to their respective mount frame $\hat{\boldsymbol{m}}_2$ axis, which matches the initial frame attitudes in the rotational deployment scenarios given in Eq. (5).

Initial Deployment Phase

During the initial deployment phase for array 1, the elements rotate together from the stowed configuration seen in Fig. 2(a) to the initial deployed configuration seen in Fig. 2(b). The elements rotate by -90 degrees about the $\hat{\boldsymbol{m}}_2$ axis during this phase. During the initial deployment phase for array 2, the array 2 elements rotate together by +90 degrees about the $\hat{\boldsymbol{m}}_2$ axis from the configuration seen in Fig. 2(c) to the initial deployed configuration seen in Fig. 2(d). Therefore, the attitude of each element frame upon completion of the initial deployment phase can be described for each array using the PRV:

$$^{\mathcal{M}_i}\boldsymbol{\gamma}_{\mathcal{F}_{ij}/\mathcal{M}_i,\text{init deploy}} = \theta_{ij,\text{init deploy}}\hat{\boldsymbol{m}}_2 = \theta_{ij,\text{init deploy}}\,{}^{\mathcal{M}_i}\begin{bmatrix}0\\1\\0\end{bmatrix} \tag{14}$$

where

$$\theta_{ij,\text{init deploy}} = 90^\circ + (-1)^i 90^\circ \tag{15}$$

Note that because the array elements purely rotate during the initial deployment phase, their translational positions remain fixed to the vectors expressed in Eq. (4).

Main Deployment Phase

During the main deployment phase, the array element frames purely translate about their respective mount frame $\hat{\boldsymbol{m}}_1$ axis. The deployment configuration for array 1 is first shown in Fig. 2(c). The final deployment configuration for both arrays is shown in Fig. 2(e). Once deployment is complete, the array element positions relative to their respective mount frame are described by the vectors:

$$^{\mathcal{M}_i}\boldsymbol{r}_{F_{ij}/M_i,\text{deploy}} = l_{ij,\text{deploy}}\,{}^{\mathcal{M}_i}\hat{\boldsymbol{t}} = l_{ij,\text{deploy}}\,{}^{\mathcal{M}_i}\begin{bmatrix}1\\0\\0\end{bmatrix} \tag{16}$$

where

$$l_{ij,\text{deploy}} = (-1)^{i+1}(j-1)L \tag{17}$$

Note that because the array elements purely translate during the main deployment phase, the element attitudes are fixed as the PRVs seen in Eq. (14).

DYNAMICS

The translational and rotational equations of motion for a space vehicle with a rigid prescribed body attached to the spacecraft hub illustrated are derived in previous work[13] and are implemented for each array element in the deployment scenarios. The equations of motion are presented in Eqs. (18) and (19) below.

$$m_{\text{sc}}\ddot{\boldsymbol{r}}_{B/N} + m_{\text{sc}}[\dot{\tilde{\boldsymbol{\omega}}}_{\mathcal{B}/\mathcal{N}}]\boldsymbol{c} = \sum \boldsymbol{F}_{\text{ext}} - m_{\text{P}}\boldsymbol{r}''_{F_c/B} - 2m_{\text{sc}}[\tilde{\boldsymbol{\omega}}_{\mathcal{B}/\mathcal{N}}]\boldsymbol{c}' - m_{\text{sc}}[\tilde{\boldsymbol{\omega}}_{\mathcal{B}/\mathcal{N}}]^2\boldsymbol{c} \tag{18}$$

$$\begin{aligned} m_{\text{sc}}[\tilde{\boldsymbol{c}}]\ddot{\boldsymbol{r}}_{B/N} + [I_{\text{sc},B}]\dot{\boldsymbol{\omega}}_{\mathcal{B}/\mathcal{N}} = \boldsymbol{L}_B - m_{\text{P}}[\tilde{\boldsymbol{r}}_{F_c/B}]\boldsymbol{r}''_{F_c/B} - \Big([I'_{\text{sc},B}] + [\tilde{\boldsymbol{\omega}}_{\mathcal{B}/\mathcal{N}}][I_{\text{sc},B}]\Big)\boldsymbol{\omega}_{\mathcal{B}/\mathcal{N}} \\ - \Big([I'_{\text{P},F_c}] + [\tilde{\boldsymbol{\omega}}_{\mathcal{B}/\mathcal{N}}][I_{\text{P},F_c}]\Big)\boldsymbol{\omega}_{\mathcal{F}/\mathcal{B}} - [I_{\text{P},F_c}]\boldsymbol{\omega}'_{\mathcal{F}/\mathcal{B}} - m_{\text{P}}[\tilde{\boldsymbol{\omega}}_{\mathcal{B}/\mathcal{N}}][\tilde{\boldsymbol{r}}_{F_c/B}]\boldsymbol{r}'_{F_c/B} \end{aligned} \tag{19}$$

Equation (18) is the translational equation of motion for the spacecraft hub point B with respect to the inertial frame. Equation (19) is the rotational equation of motion for the spacecraft system. These vector equations are frame-independent and general so that they can be used to represent a wide range of spacecraft configurations.

SOFTWARE IMPLEMENTATION

Recall that simulation of the deployment scenarios requires profiling the states of each individual solar array element relative to the spacecraft hub. Because the array elements are assumed to be acting according to *prescribed motion*, no individual equations of motions exist for the array elements. Rather, the sub-effector motion states are prescribed kinematic translational and rotational states which couple with the spacecraft hub motion. This creates a general nonlinear spacecraft dynamics modeling solution where the deployment of multiple sub-components can be modeled. Therefore, kinematic profilers must be developed to prescribe the required translational or rotational motion for each array element with respect to the spacecraft hub frame. Note that strict discretion must be taken to ensure the profiled motion is admissible and does not violate any fundamental laws of physics.

Previous work[13] developed two kinematic profiler modules in Basilisk for this purpose. The first module profiled translational motion along a fixed axis in the mount frame, while the second module profiled a rotation about a fixed axis in the mount frame. The Basilisk `messaging` system is used as an interface to relay the profiled states at each time step from the profiler modules to the prescribed motion dynamics module. A diagram illustrating the required Basilisk modules and their connections for each *individual* array element is presented in Fig. (5).

This work enhances the previously developed translational and rotational profiler modules to profile the motion of each array element. The following two sections discuss these profiler modules in greater detail.

Rotational Motion Profiler

The rotational motion profiler developed in previous work[13] applies a bang-bang angular acceleration profile to the prescribed body that results in the fastest possible single degree-of-freedom rotation from a rest-to-rest state. As a result of this acceleration profile, the prescribed body's angular rotation rate changes linearly in time and reaches a maximum magnitude halfway through the rotation. The resulting angular motion during the rotation is parabolic in time.

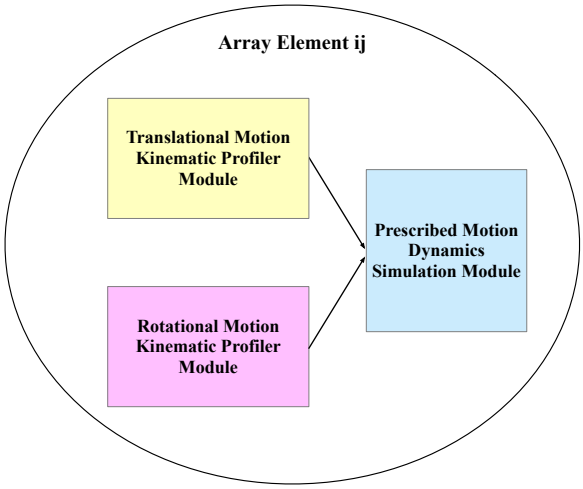

Figure 5. Required simulation modules for each individual array element.

In this work, the rotational profiler is enhanced with a coast option added to the module where a period of zero acceleration is added between the acceleration segments. The user is given the option to configure how long the acceleration ramp segments are applied using a `tRamp` variable. Using this profiler for each deployment phase, the array elements are configured to move at a constant rate for nearly the entire deployment phase. In this work, the length of each deployment phase is chosen and used with the specified `tRamp` variable to solve for the required element accelerations.

First, the length of the coast period during each deployment phase is found using the simple expression:

$$t_{\text{coast}} = t_{\text{deploy}} - 2t_{\text{ramp}} \tag{20}$$

Note that because each individual array has two deployment phases and four scenarios are simulated, there are a total of 16 deployment phases. Ultimately, each of the 16 phases can have different specified values for both t_{deploy} and t_{ramp}. In this work, the deployment parameters are identical for each array, reducing the number of unique values for each of these parameters to 8. The specific values chosen for each phase are outlined in the software implementation section of this paper. The next sections discuss how the ramp segment accelerations for each element are found for each phase of the deployment scenarios.

Rotational Rigid Deployment

For each phase of the rotational rigid deployment scenario, all array elements are given the same profiled motion; however the only exception to this behavior is during the main deployment phase. The elements move together until each element sequentially arrives to their final deployed orientation. Therefore, at the end of deployment only the last array element is in motion while all others are locked in place.

The required acceleration magnitude for each element during the initial deployment phase is found as:

$$\alpha_{ij,\text{init deploy}} = \frac{|\theta_{ij,\text{init deploy}} - \theta_{ij,\text{stowed}}|}{t_{\text{coast}} t_{\text{ramp}} + t_{\text{ramp}}^2} \tag{21}$$

The required angular acceleration magnitude for each element during the main deployment phase is

found as:

$$\alpha_{ij,\text{deploy}} = \frac{360^\circ/N}{t_{\text{coast}}t_{\text{ramp}} + t_{\text{ramp}}^2} \tag{22}$$

Note that after each element arrives to its final deployed orientation, the angular acceleration and angular velocity of the element is set to zero.

Rotational Lanyard Deployment

For the rotational lanyard deployment scenario, the array elements are given unique angular accelerations during the main deployment phase in order to arrive at their final deployed orientations at the same time. During the initial deployment phase the array elements are given the same angular acceleration value specified in Eq. (21).

The required angular acceleration magnitude for each element during the main deployment phase is found as:

$$\alpha_{ij,\text{deploy}} = \frac{|\theta_{ij,\text{deploy}} - \theta_{ij,\text{init deploy}}|}{t_{\text{coast}}t_{\text{ramp}} + t_{\text{ramp}}^2} \tag{23}$$

Translational Motion Profiler

Similar to the rotational motion profiler developed in previous work,[13] the translational motion profiler also applies a bang-bang acceleration profile to the prescribed body; however the profile is purely translational along a single mount frame axis. The resulting velocity of the prescribed body relative to the hub is linear in time and reaches a maximum magnitude halfway through the translation. The translational motion of the body is therefore parabolic in time.

In this work, the translational profiler is also enhanced with a coast option added to the module. The user configures the duration of the acceleration segments using the `tRamp` variable. This addition to the profiler module more realistically reflects how the individual elements move during deployment. Using this profiler for each deployment phase, the array elements are configured to move at a constant rate for nearly the entire deployment phase. The length of each deployment phase is chosen in this work and the expression in Eq. (20) is used to calculate the duration of each coast period. The next sections discuss how the ramp segment accelerations for each element are found for each phase of the deployment scenarios.

Telescoping Rigid Deployment

For the initial deployment phase of the telescoping rigid deployment scenario, all array elements rotate together and are given the same profiled motion. During the main deployment phase, the array elements are given the same acceleration values when they begin to move away from the spacecraft hub. The array elements remain fixed in the initial deployed configuration during the main deployment phase and individually telescope away from the spacecraft hub until the panel is fully deployed.

The required angular acceleration magnitude for each element during the initial deployment phase is found as:

$$\alpha_{ij,\text{init deploy}} = \frac{|\theta_{ij,\text{init deploy}} - \theta_{ij,\text{stowed}}|}{t_{\text{coast}}t_{\text{ramp}} + t_{\text{ramp}}^2} \tag{24}$$

The required linear acceleration magnitude for each element during the main deployment phase is found as:

$$a_{ij,\text{deploy}} = \frac{L}{t_{\text{coast}}t_{\text{ramp}} + t_{\text{ramp}}^2} \tag{25}$$

Note that the linear acceleration and velocity of each element is fixed at zero until the element begins telescoping away from the spacecraft hub.

Telescoping Lanyard Deployment

For the rotational lanyard deployment scenario, the array elements are given unique linear accelerations during the main deployment phase in order to arrive to their final deployed orientations at the same time. During the initial deployment phase the array elements are given the same angular acceleration value specified in Eq. (24).

The required linear acceleration magnitude for each element during the main deployment phase is found as:

$$a_{ij,\text{deploy}} = \frac{l_{ij,\text{deploy}}}{t_{\text{coast}} t_{\text{ramp}} + t_{\text{ramp}}^2} \tag{26}$$

RESULTS

Simulation Setup

All simulations in this work set up an initially non-rotating spacecraft hub with a mass of 800 kilograms. The spacecraft is not placed into any orbit and no gravitational bodies are added to the scenarios. The hub body frame is initially aligned with the inertial reference frame. The relevant simulation parameters for the deployment scenarios are provided in Tables (1-3). The hub-specific parameters are given in Table (1) while the parameters for the rotational and telescoping scenarios are given in Tables (2) and (3), respectively. A complete list of the scenario parameters can be found on github[†].

Rotational Deployment Results

Rotational Rigid Deployment

The simulation results for the rotational rigid deployment scenario are presented in Figs. (6) and (7). Figure (6) presents the scalar element angles and angle rates for both arrays relative to the hub while Fig. (7) presents the resulting hub dynamics due to the deployment. Viewing Figs. 6(a), array 1 is seen to first rotate +90 degrees during the initial deployment phase. After this initial rotation, the array elements begin the main deployment phase and rotate together while sequentially locking into their final deployed configurations. Array 1 element 1 does not rotate during the main deployment phase. Fig. 6(b) illustrates array 2 deploying with symmetric behavior only after array 1 completes its deployment.

Fig. 7(a) presents the hub inertial angular velocity. The hub rate about the $\hat{\boldsymbol{b}}_2$ axis is seen to vary with a maximum value occurring after array 1 completes the initial deployment phase. The hub rates about the $\hat{\boldsymbol{b}}_1$ and $\hat{\boldsymbol{b}}_3$ axes are seen to remain near zero throughout the entire deployment. During the main deployment phases, the second hub angular velocity component is seen to jump consistently during the acceleration ramp segments for each element. This behavior is expected, as the hub must respond to conserve the spacecraft angular momentum. The conservation of angular momentum is evident from the hub returning to a resting state at the end of the deployment scenario. Considering Figs. 7(b) and 7(c), the hub inertial attitude and position are seen to shift appropriately during each phase of deployment. During the deployment of array 1 in the X-Z hub plane, the hub is

[†] `https://github.com/leahkiner/sc-dynamics-sim/tree/conferences/aas-gnc-feb-2024`

Table 1. Shared scenario parameters.

Parameter	Value	Unit
m_{hub}	800.0	kg
${}^{\mathcal{B}}[I_{\text{hub},B_c}]$	$\begin{bmatrix} 333.33 & 0.0 & 0.0 \\ 0.0 & 333.33 & 0.0 \\ 0.0 & 0.0 & 133.33 \end{bmatrix}$	kg $\cdot$ m^2
$\boldsymbol{r}_{B_c/B}$	[0.0, 0.0, 0.0]	m
${}^{\mathcal{B}}\boldsymbol{\omega}_{\mathcal{B}/\mathcal{N}}(t_0)$	[0.1, 0.1, 0.1]	deg/s
$\boldsymbol{\sigma}_{\mathcal{B}/\mathcal{N}}(t_0)$	[0.0, 0.0, 0.0]	N/A
${}^{\mathcal{M}_i}\boldsymbol{\omega}_{\mathcal{M}_i/\mathcal{B}}$	[0.0, 0.0, 0.0]	deg/s
$\boldsymbol{\sigma}_{\mathcal{M}_i/\mathcal{B}}$	[0.0, 0.0, 0.0]	N/A
${}^{\mathcal{M}_i}\hat{\boldsymbol{s}}$	[0.0, 1.0, 0.0]	N/A
$t_{\text{init deploy}}$	5.0	min
t_{deploy}	20.0	min
t_{ramp}	1.0	s

Table 2. Rotational scenario parameters.

Parameter	Value	Unit
N	10	N/A
R	3.0	m
m_{element}	8.0	kg
${}^{\mathcal{F}}[I_{\text{Element},F_c}]$	$\begin{bmatrix} 6.00167 & 0.0 & 0.0 \\ 0.0 & 8.2918 & 0.0 \\ 0.0 & 0.0 & 2.2935 \end{bmatrix}$	kg $\cdot$ m^2
${}^{\mathcal{B}}\boldsymbol{r}_{M_1/B}$	[0.5, 0.0, 0.5]	m
${}^{\mathcal{B}}\boldsymbol{r}_{M_2/B}$	[-0.5, 0.0, 0.5]	m

Table 3. Telescoping scenario parameters.

Parameter	Value	Unit
N	5	N/A
L	2.0	m
${}^{\mathcal{M}_i}\hat{\boldsymbol{t}}$	[1.0, 0.0, 0.0]	N/A
m_{element}	10.0	kg
${}^{\mathcal{F}}[I_{\text{Element},F_c}]$	$\begin{bmatrix} 3.3354 & 0.0 & 0.0 \\ 0.0 & 3.8021 & 0.0 \\ 0.0 & 0.0 & 0.4708 \end{bmatrix}$	$\text{kg} \cdot \text{m}^2$
${}^{\mathcal{B}}\boldsymbol{r}_{M_1/B}$	[0.5, 0.0, 1.0]	m
${}^{\mathcal{B}}\boldsymbol{r}_{M_2/B}$	[-0.5, 0.0, 1.0]	m

seen to compensate by both translating and rotating negatively in the inertial X-Z plane. During the deployment of array 2 in the X-Z hub plane, the hub appropriately translates and rotates positively in the inertial X-Z plane.

Rotational Lanyard Deployment

Figs. (8) and (9) present the simulation results for the rotational lanyard deployment scenario. Figure (8) presents the scalar element angles and angle rates for both arrays relative to the hub while Fig. (9) presents the resulting hub dynamics due to the deployment. Identical to the rotational rigid deployment scenario, Figs. 8(a) shows all elements of array 1 rotating +90 degrees during the initial deployment phase. During the main deployment phase, all elements begin to move simultaneously and arrive to their final deployed orientations at the same instant as compared to the rigid scenario. Considering Fig. 8(b), array 2 is seen to deploy with symmetric behavior only after array 1 completes its deployment.

Viewing Fig. (9), the hub motion during both array deployments is seen to closely match the results seen in the rotational rigid deployment. The hub attitude and inertial position results in Figs. 9(b) and 9(c) are nearly identical to the results in Figs. 7(b) and 7(c). Considering Fig. 9(a), it is interesting to see that the hub rate is much smoother throughout the entire deployment than seen in Fig. 7(a). The hub behavior during the initial deployment of array 1 is identical between these two scenarios; however for the lanyard deployment all array elements are given an acceleration at the start of the main deployment phase. The smooth hub motion during the main lanyard deployment phase is a result of all array elements moving at constant rates throughout most of this phase.

Telescoping Deployment Results

Telescoping Rigid Deployment

The simulation results for the telescoping rigid deployment scenario are presented in Figs. (10) and (11). Figure (10) presents the scalar element displacements and rotation angles for both arrays relative to the hub while Fig. (11) presents the resulting hub dynamics due to the deployment. Considering Figs. 10(a) and 10(c), array 1 is seen to first rotate -90 degrees while all elements remain fixed to the hub with zero displacement. After the initial rotation is complete, the array elements are

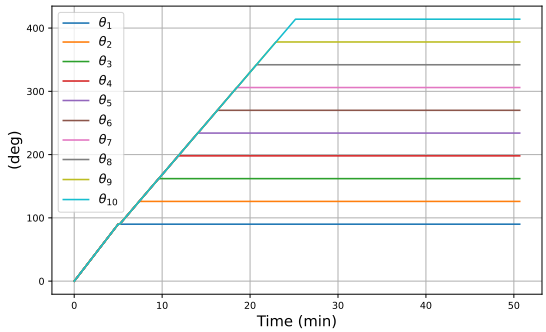

(a) Array 1 element angles.

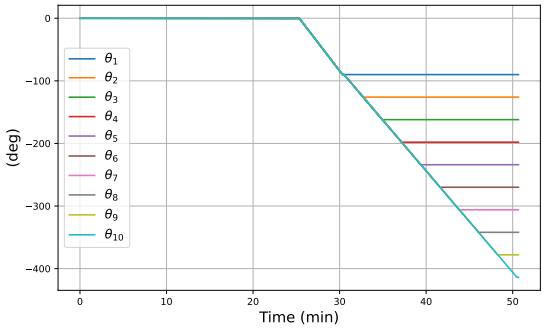

(b) Array 2 element angles.

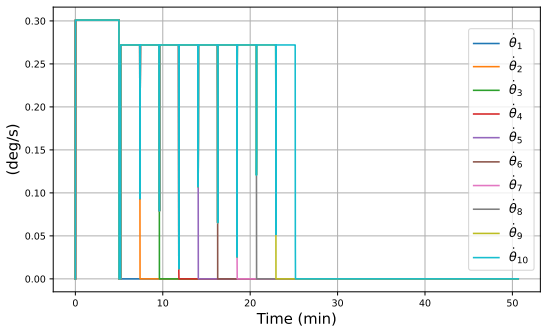

(c) Array 1 element angle rates.

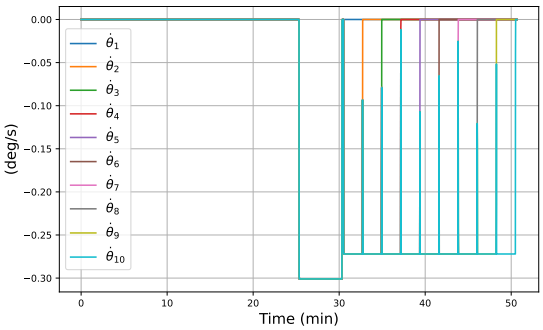

(d) Array 2 element angle rates.

Figure 6. Profiled array element rotational states for the rotational rigid deployment scenario.

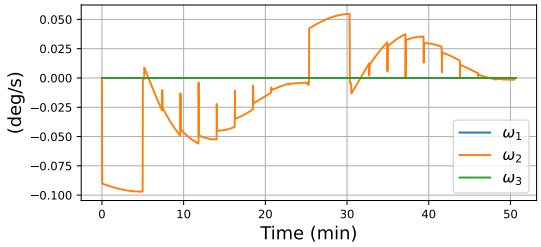

(a) Hub inertial angular velocity.

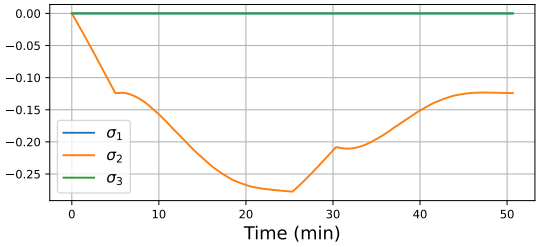

(b) Hub inertial attitude.

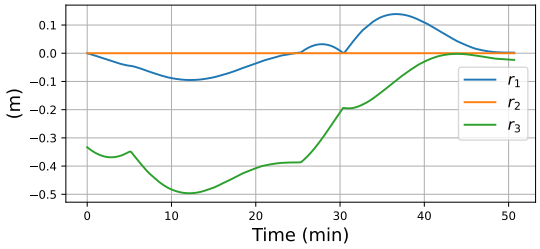

(c) Hub inertial position.

Figure 7. Hub inertial states for the rotational rigid deployment scenario.

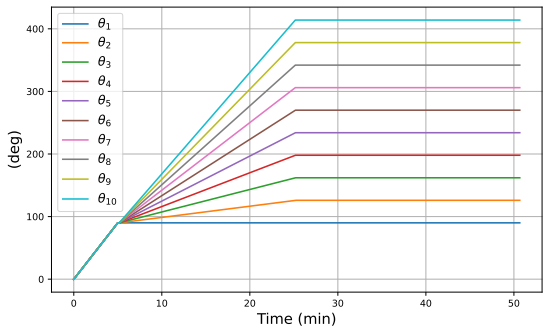

(a) Array 1 element angles.

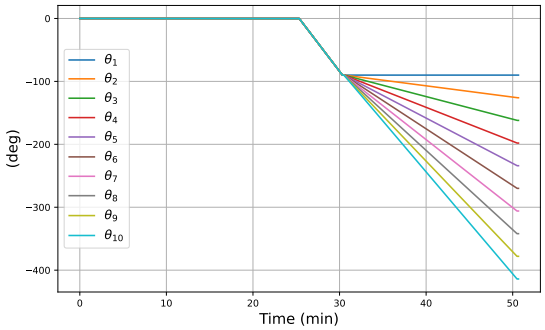

(b) Array 2 element angles.

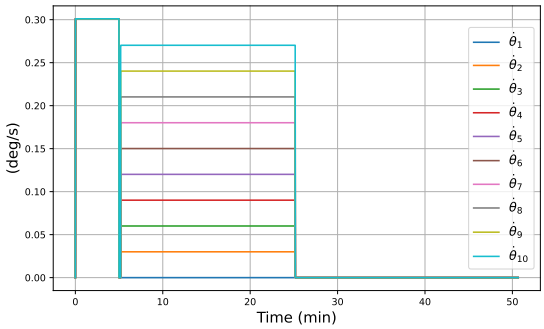

(c) Array 1 element angle rates.

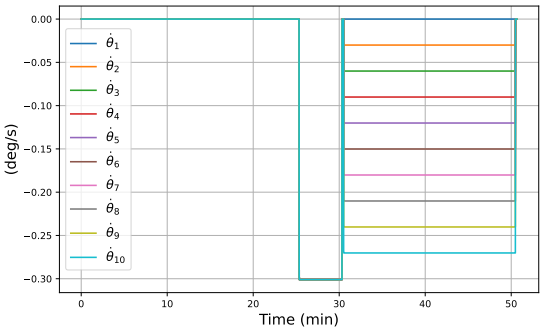

(d) Array 2 element angle rates.

Figure 8. Profiled array element rotational states for the rotational lanyard deployment scenario.

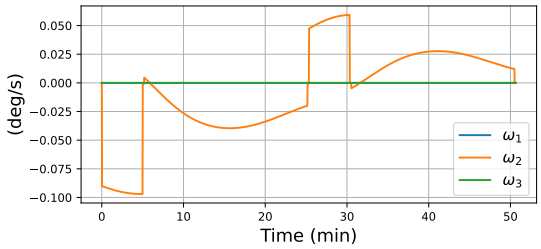

(a) Hub inertial angular velocity.

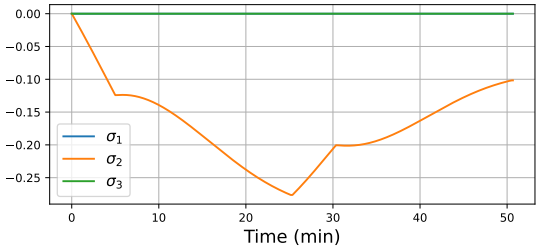

(b) Hub inertial attitude.

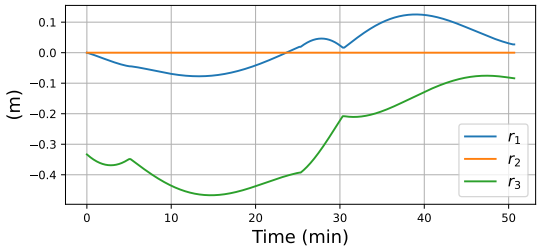

(c) Hub inertial position.

Figure 9. Hub inertial states for the rotational lanyard deployment scenario.

seen to translate away from the hub with positive displacements while the array rotational motion remains fixed. The array elements remain fixed to the hub until they sequentially begin deploying to their final positions in intervals of the element length L. Array 1 element 5 does not translate during the main deployment phase. Viewing Figs. 10(b) and 10(d), array 2 is seen to deploy with symmetric behavior only after array 1 completes its deployment.

The hub inertial angular velocity is presented in Fig. 11(a). The hub rate about the $\hat{\boldsymbol{b}}_2$ axis is seen to vary with a maximum value occurring after array 1 completes the initial deployment phase. The hub rates about the $\hat{\boldsymbol{b}}_1$ and $\hat{\boldsymbol{b}}_3$ axes are seen to remain near zero throughout the entire deployment. During the main deployment phases, the $\hat{\boldsymbol{b}}_2$ angular velocity component is seen to jump consistently during the acceleration ramp segments for each element. This behavior is expected, as the hub must respond to conserve the spacecraft angular momentum. The conservation of angular momentum is evident from the hub returning to a resting state at the end of the deployment scenario. Considering Fig. 11(c), the hub inertial position is seen to shift appropriately during each phase of deployment. During the deployment of array 1 along the hub +X axis, the hub is seen to move along the inertial -X direction. During the deployment of array 2 along the hub -X axis, the hub is seen to shift along the inertial +X direction. During the initial deployment phase for each array, the hub position is also seen to shift along the inertial -Z direction which is a result of the array rotational motion in the hub X-Z plane.

Telescoping Lanyard Deployment

Figs. (12) and (13) display the simulation results for the telescoping lanyard deployment scenario. Figure (12) presents the scalar element displacements and rotation angles for both arrays relative to the hub while Fig. (13) presents the resulting hub dynamics due to the deployment. Identical to the telescoping rigid deployment scenario, Figs. 12(a) and 12(b) show array 1 rotating -90 degrees during the initial deployment phase while all elements remain fixed to the hub with zero displacement. After the initial rotation, the array elements begin to translate away from the hub simultaneously as compared to the rigid scenario. The elements are seen to lock into their final deployed locations at the same instant in this scenario. Array 1 element 1 does not translate during the main deployment phase. Viewing Figs. 12(b) and 12(d), array 2 is seen to deploy with symmetric behavior only after array 1 completes its deployment.

The hub motion displayed in Fig. (13) is seen to closely match the results seen in the telescoping rigid deployment. The hub attitude and inertial position results in Figs. 13(b) and 13(c) are nearly identical to the results in Figs. 11(b) and 11(c). Considering Fig. 13(a), it is interesting to see that the hub rate is much smoother throughout the entire deployment than seen in Fig. 11(a). The hub behavior during the initial deployment of array 1 is identical between these two scenarios; however for the lanyard deployment all array elements are given an acceleration at the start of the main deployment phase. This results in a larger change in the hub rate at a simulation time of 5 minutes compared to the rigid scenario. The smooth hub motion during the main lanyard deployment phase is due to all array elements moving at constant rates throughout most of this phase.

Hub Body Rate Comparison Across Scenarios

The inertial angular velocity of the spacecraft hub is a key state used for verifying that mission requirements are met across the lifespan of a mission. A rate limit is often chosen that must not be exceeded by the craft or the onboard fault protection system will be triggered. If the spacecraft is directed to go into a safe state configuration until the rate is reduced, any number of the mission

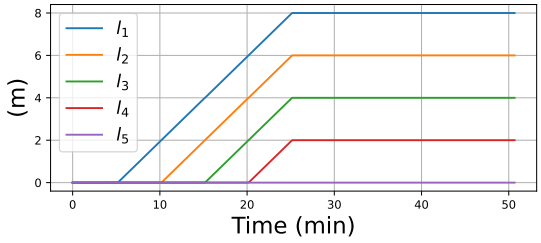

(a) Array 1 element positions.

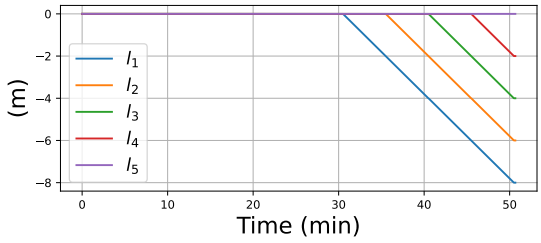

(b) Array 2 element positions.

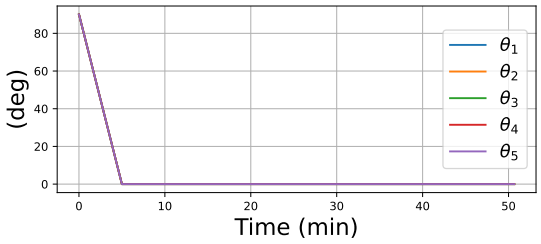

(c) Array 1 element angles.

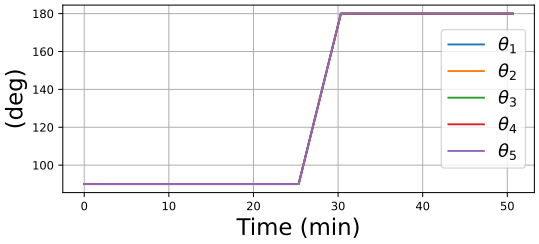

(d) Array 2 element angles.

Figure 10. Profiled array element states for the telescoping rigid deployment scenario.

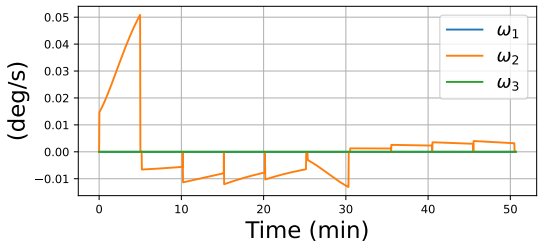

(a) Hub inertial angular velocity.

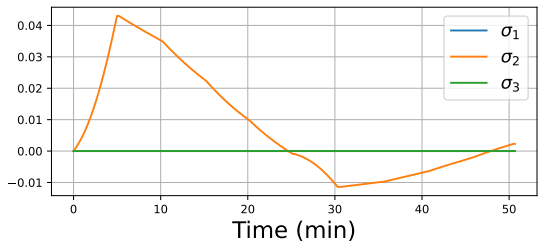

(b) Hub inertial attitude.

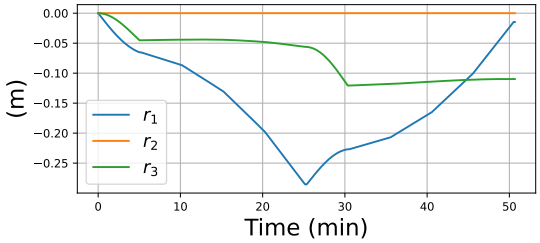

(c) Hub inertial position.

Figure 11. Hub inertial states for the telescoping rigid deployment scenario.

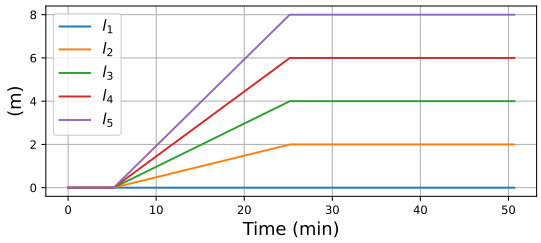

(a) Array 1 element positions.

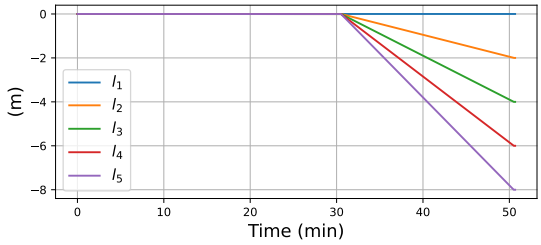

(b) Array 2 element positions.

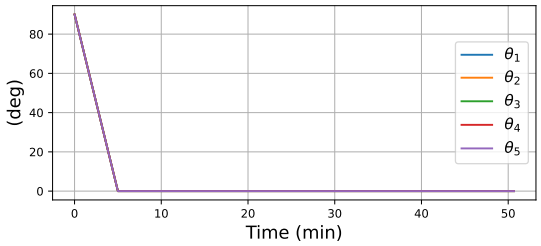

(c) Array 1 element angles.

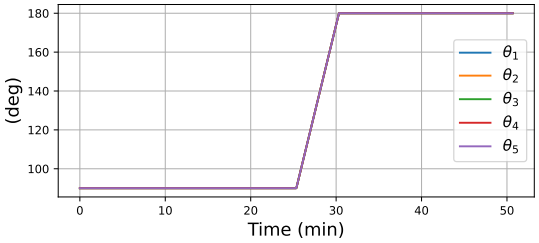

(d) Array 2 element angles.

Figure 12. Profiled array element states for the telescoping lanyard deployment scenario.

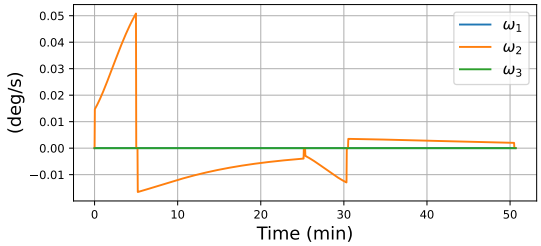

(a) Hub inertial angular velocity.

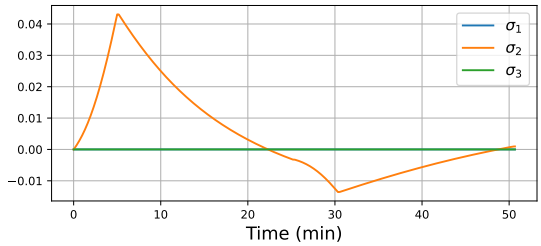

(b) Hub inertial attitude.

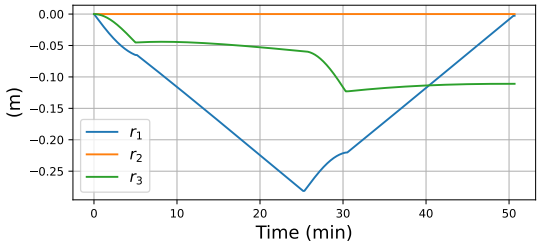

(c) Hub inertial position.

Figure 13. Hub inertial states for the telescoping lanyard deployment scenario.

science objectives may be compromised. For this reason, it is of interest to compare the inertial hub angular velocity across the different deployment scenarios. To do so, the magnitude of the hub rate is plotted for each deployment scenario in Fig. (14).

Viewing Fig. (14), it is clear that the hub rate does not exceed 0.1 degrees per second for all deployment scenarios. This upper bound is well below nominal hub rate limits of 2 degrees. As expected, the rigid and lanyard deployment results for each scenario begin to noticeably diverge after the initial deployment phase for array 1 where the hub rates are identical. While the lanyard deployments have much smoother impacts on the hub rate, the rigid deployments cause the hub rate to spike during the acceleration phases for each array element. It is interesting to see that neither the rigid or lanyard deployments have an overall larger impact on the hub rate for both deployment scenarios. For the rotational scenario, the hub rate transitions about halfway through the main deployment phase for each array from being larger in the rigid deployment to being larger in the lanyard deployment. The converse is true when examining the hub rate for the telescoping deployment scenarios.

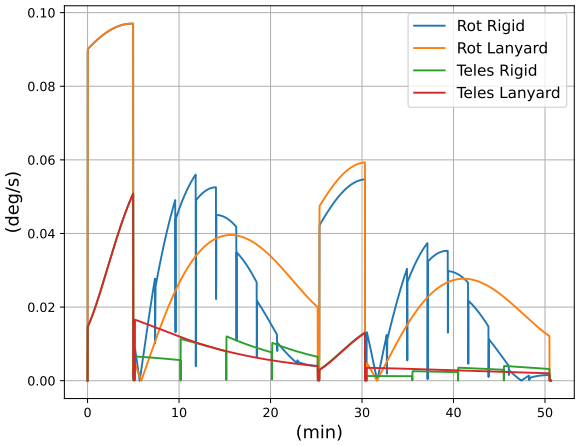

Figure 14. Spacecraft hub body rate magnitude for each deployment scenario.

CONCLUSION

The ability to extensively simulate complex space vehicles before mission launch is crucial for mission success. With the growing complexity of appendages attached to the central spacecraft hub such as deploying articulable solar arrays and multi-link robotic manipulator arms, accurately modeling the dynamics of these complex structures and analyzing their impact on the spacecraft hub dynamics becomes increasingly more valuable to ensure confidence and reliability in the selected spacecraft design.

This paper introduces a method to simulate a variety of solar array deployment scenarios utilizing the Basilisk astrodynamics simulation software framework. By considering each solar array as a collection of N connected rigid elements, the previously developed prescribed motion dynamics module is used to simulate the dynamics of each element acting on the spacecraft hub. N instances of both the translational and rotational kinematic profiler modules are enhanced to profile the kinematic states of each array element relative to the spacecraft hub. The dynamical impact of several array deployment configurations on the spacecraft hub is shown and compared for each deployment scenario. The development of these general software tools enables a more accessible, rapid

approach to simulating and analyzing complex time-varying spacecraft geometries.

REFERENCES

[1] J. R. Brophy, "NASA's Deep Space 1 Ion Engine (Plenary)," *Review of Scientific Instruments*, Vol. 73, No. 2, 2002, pp. 1071–1078.

[2] B. N. M. M. M. H. J. Brophy, C. Garner and D. Noon, "General Hinged Rigid-Body Dynamics Approximating First-Order Spacecraft Solar Panel Flexing," *The Ion Propulsion System for Dawn*, Vol. 55, 2003, p. 4542.

[3] T. D. W. H. T. I. e. a. D. Y. Oh, S. Collins, "Development of the Psyche Mission for NASA's Discovery Program," *36th International Electric Propulsion Conference*, University of Vienna, Vienna Austria, Sep. 15–20 2019. Paper No. IEPC-2019-192.

[4] J. S. Sovey, V. K. Rawlin, and M. J. Patterson, "Ion Propulsion Development Projects in U.S.: Space Electric Rocket Test I to Deep Space 1," *Journal of Propulsion and Power*, Vol. 17, No. 3, 2001, pp. 517–526, 10.2514/2.5806.

[5] R. Calaon, L. Kiner, C. Allard, and H. Schaub, "Momentum Management Of A Spacecraft Equipped With A Dual-Gimballed Electric Thruster," *AAS Guidance and Control Conference*, Breckenridge, CO, Feb. 2–8 2023. Paper No. AAS-23-178.

[6] J. Vaz Carneiro, C. Allard, and H. Schaub, "Rotating Rigid Body Dynamics Architecture For Spacecraft Simulation Software Implementation," *AAS Guidance and Control Conference*, Breckenridge, CO, Feb. 2–8 2023. Paper No. AAS-23-112.

[7] R. G. D. B. A. Aikenhead and F. M. Davis, "Canadarm and The Space Shuttle," *Journal of Vacuum Science and Technology A: Vacuum, Surfaces, and Films*, Vol. 1, No. 2, 1983, pp. 126–132.

[8] S. Sachdev, "Canadarm- a review of its flights," *Journal of Vacuum Science and Technology A: Vacuum, Surfaces, and Films*, Vol. 4, No. 3, 1986, pp. 268–272.

[9] K. B. M. Hiltz, C. Rice and R. Allison, "Canadarm: 20 years of mission success through adaptation," *International Symposium on Artificial Intelligence, Robotics and Automation*, University of Vienna, Vienna Austria, 2001. Paper No. JSC-CN-6877.

[10] C. R. Mercer, "Chapter Twelve - Solar array designs for deep space science missions," *Photovoltaics for Space* (S. G. Bailey, A. F. Hepp, D. C. Ferguson, R. P. Raffaelle, and S. M. Durbin, eds.), pp. 349–378, Elsevier, 2023, https://doi.org/10.1016/B978-0-12-823300-9.00006-6.

[11] B. G. Özdemir, "Power stage design and implementation of a deploymentmechanism driver for space applications," Master's thesis, Middle East Technical University, 2012.

[12] J. Sun, "A New Design of the 3D Deployable Solar Array in the Aerospace Field and Kinematic Analysis during Deployment," *Journal of Physics: Conference Series*, Vol. 2364, nov 2022, p. 012039, 10.1088/1742-6596/2364/1/012039.

[13] L. Kiner, J. V. Carneiro, C. Allard, and H. Schaub, "Spacecraft Simulation Software Implementation of General Prescribed Motion Dynamics of Two Connected Rigid Bodies," AAS Rocky Mountain GN&C Conference, Breckenridge, CO, Feb. 2–8, 2023.

[14] G. Bascom, L. Kiner, and H. Schaub, "Spacecraft Dynamics Analysis Using Stochastic Point-Mass Model of Human Motion," AAS/AIAA Space Flight Mechanics Meeting, Austin, TX, Jan. 15–19, 2023.

[15] H. Schaub and J. L. Junkins, *Analytical Mechanics of Space Systems*. Reston, Virginia: American Institute of Aeronautics and Astronautics, Inc., 4 ed., 2018.